Commun. Comput. Phys.
doi: 10.4208/cicp.090813.160414a

Vol. **16**, No. 4, pp. 1031-1055
October 2014

Hydrodynamic Interaction of Elastic Capsules in Bounded Shear Flow

D. V. Le[1] and Zhijun Tan[2,3,*]

[1] *Institute of High Performance Computing, Agency for Science, Technology and Research, 1 Fusionopolis Way, #16-16 Connexis, Singapore 138632.*
[2] *School of Mathematics and Computational Science, Sun Yat-sen University, Guangzhou 510275, China.*
[3] *Province Key Laboratory of Computational Science, Sun Yat-sen University, Guangzhou 510275, China.*

Received 9 August 2013; Accepted (in revised version) 16 April 2014

Communicated by Boo-Cheong Khoo

Available online 8 August 2014

Abstract. This paper presents a modified Loop's subdivision algorithm for studying the deformation of a single capsule, the hydrodynamic interaction between two capsules and the hydrodynamic diffusion of a suspension of capsules in bounded shear flow. A subdivision thin-shell model is employed to compute the forces generated on the surface of the elastic capsule during deformation. The capsule surface is approximated using the modified Loop's subdivision scheme which guarantees bounded curvature and C^1 continuity everywhere on the limit surface. The present numerical technique has been validated by studying the deformation of a spherical capsule in shear flow. Computations are also performed for a biconcave capsule over a wide range of shear rates and viscosity ratios to investigate its dynamics. In addition, the hydrodynamic interaction between two elastic capsules in bounded shear flow is studied. Depending on the wall separation distance, the trajectory-bifurcation points that separate reversing and crossing motions for both spherical and biconcave capsules can be found. Compared to the spherical capsules, the biconcave capsules exhibit additional types of interaction such as rotation and head-on collision. The head-on collision results in a large trajectory shift which contribute to the hydrodynamic diffusion of a suspension. A suspension of a large number of biconcave capsules in shear flow is also simulated to show the ability of the modified scheme in running a large-scale simulation over a long period of time.

AMS subject classifications: 65M06, 76D05, 74F10, 92C10

Key words: Thin shell, elastic capsules, red-blood cells, subdivision surfaces, immersed boundary method, Navier-Stokes equations.

*Corresponding author. *Email addresses:* ledv@ihpc.a-star.edu.sg (D. V. Le), tzhij@mail.sysu.edu.cn (Z. Tan)

1 Introduction

In recent years, the interest in particle motion has been motivated by applications in microfluidics and cell biomechanics. Numerous studies have been performed theoretically, computationally and experimentally for liquid droplets, elastic capsules and red blood cells [2, 11, 13, 36] to understand how their behaviors affect the flow characteristics. The motion of a single spherical and slender rigid particle has been well understood. The dynamics of an isolated elastic capsule or single cell in shear flow is also relatively well known. In a simple shear flow, spherical capsules exhibit a stationary tank-treading behavior [32] while spheroidal and biconcave capsules undergo swinging or tumbling motion [1]. The dynamics of the capsule depends on the viscosity ratio between the internal and suspending fluids, applied shear rate and the elastic properties of the capsule membrane. These parameters also affect the hydrodynamics interaction between two particles in shear flow.

The simplest of problems concerning the interaction between two particles has been considered for a pair of neutrally buoyant rigid spheres [3, 9, 17]. The analysis of Batchelor and Green [3] showed that, depending on the separation distance between the two spheres, they will either orbit around each other or passing each other before returning to their initial transverse positions. This result is in agreement with the experiment studied in [9] for the interaction of two rigid spheres in Couette flow. Recently, Pozrikidis [30, 31] developed accurate numerical methods for simulating the interception of two spherical particles with arbitrary radii in simple shear flow and discussed the particle self-diffusivities.

Unlike the interaction of two smooth rigid spheres, the hydrodynamic interaction between two liquid droplets results in an irreversible vertical displacement [5, 24] which leads to shear-induced diffusion in a suspension of liquid particles. Such irreversible shift in the particle trajectories has also been observed for liquid capsules [4, 10, 18, 19]. Depending on the initial separation distance, the two spherical capsules in shear flow either cross over each other or undergo reversing motion as observed in [10]. The reversing motion, in which the two capsules reversed their directions of motion upon approaching, is the result of the wall effect in the cross-flow direction. In this article, we investigate numerically the hydrodynamic interactions between two identical spherical capsules and red-blood cells in bounded shear flow and study the effects of channel heights on the reversing motion. We also investigate numerically the hydrodynamic interactions of a large number of biconcave capsules in a dense suspension to study the hydrodynamic diffusion or shear-induced diffusion. Hydrodynamic diffusion of capsules in a suspension is a phenomenon in which capsules exhibit diffusive motion during flow due to the interactions between them. This motion is responsible for phenomena such as blood viscosity changes in small capillaries and the natural propensity for blood cells to migrate to certain preferred locations within a conduit, which is an important application of this phenomenon. For example, taking advantage of the tendency for white blood cells to marginate in long channels, it is possible to design a microfluidic device for separating

white blood cells directly from other components of the whole blood. It is also possible to use the diffusion information to find new and possibly important differences between the blood from healthy patients and the blood from patients with blood cell disorder [15].

In the present numerical study, a front tracking method with subdivision thin-shell model similar to that in [20, 21] is employed for handling the deformation and interaction of the elastic capsules. In literature, the kinematics of deformation of the capsule membranes have been handled by different membrane models with different membrane discretization. A finite element model with linear triangular element [6,33] has been used in [12, 23, 38] to calculate the forces the membrane applied to the fluid during the deformation. Alternatively, an elastic membrane model with quadratic triangular element developed in Cartesian coordinates [32] has been employed in [29] to take full account of in-plane tensions and bending moments generated during capsule deformation. Recently, a thin-shell model [7, 8] with Loop's subdivision surface [26] has been employed in [16, 21] for computing stress and moment resultants on an unstructured triangular mesh representing the capsule surface. Subdivision surfaces obtained by the Loop's scheme are guaranteed to be C^2-continuous everywhere except in the immediate vicinity of a small number of vertices in the control mesh where they still retain C^1 continuity. While the original Loop's subdivision algorithm has proven to be a valuable tool for modeling arbitrary surfaces, the surfaces generated by the original scheme [26] may have unbounded curvature. This defect can be removed by introducing the modified Loop's algorithm [25] with subdivision masks that obey bounded curvature constraints and the convex-hull property. It should be noted that the original Loop's subdivision scheme worked very well for a single capsule in shear flow [20,21]. However, it may suffer from the instability after a long period of time in the simulations of a large number of interacting capsules. When multiple capsules approach each other, the sections of the capsule membranes surrounding the lubrication layer experience a drastic build-up in pressure. As a result, the Lagrangian meshes representing the membranes may experience huge distortion. When the distortion is large, the original Loop's subdivision scheme may cause large errors in the calculated curvature and membrane force, which in turn leads to numerical instability. Therefore, in the present work the modified Loop's subdivision surface [25] with bounded curvature property is employed for computing the forces generated on the capsule surfaces during the deformation and hydrodynamic interaction of elastic capsules in bounded shear flow.

2 Formulation

2.1 Governing equations

In a 3-dimensional bounded fluid domain Ω_F, the incompressible Navier-Stokes equations is considered, which is written as

$$\rho(\boldsymbol{u}_t+(\boldsymbol{u}\cdot\nabla)\boldsymbol{u})=-\nabla p+\nabla\cdot\left[\mu\left(\nabla\boldsymbol{u}+\nabla\boldsymbol{u}^T\right)\right]+\boldsymbol{f}, \tag{2.1}$$

$$\nabla\cdot\boldsymbol{u}=0, \tag{2.2}$$

where $\boldsymbol{u}=(u,v,w)^T$ is the fluid velocity, p the pressure, and ρ and μ the density and viscosity of the fluid, respectively. The effect of the thin shell with middle surface $\Gamma(t)$ immersed in the fluid results in a singular force

$$\boldsymbol{f}(\boldsymbol{x},t)=\int_{\Gamma(t)}\boldsymbol{f}^s(\xi^1,\xi^2,t)\delta(\boldsymbol{x}-\boldsymbol{X}(\xi^1,\xi^2,t))\mathrm{d}\Gamma, \tag{2.3}$$

where $\boldsymbol{X}(\xi^1,\xi^2,t)$ is a control point associated with the curvilinear coordinates (ξ^1,ξ^2) on the shell middle surface and $\boldsymbol{f}^s(\xi^1,\xi^2,t)$ is the force per unit area at time t. Here, $\boldsymbol{x}=(x,y,z)$ is spatial position and $\delta(\boldsymbol{x})$ is the three-dimensional Dirac function. The shell follows the local fluid velocity as

$$\frac{\mathrm{d}\boldsymbol{X}(t)}{\mathrm{d}t}=\int_{\Omega_F}\boldsymbol{u}(\boldsymbol{x},t)\delta(\boldsymbol{x}-\boldsymbol{X}(t))\mathrm{d}\boldsymbol{x}. \tag{2.4}$$

2.2 Thin shell formulation

For the sake of completeness, the kinematic description and equilibrium deformations of the hyperelastic shells are summarized in this section. Further details can be found in [7,8,21]. Consider a shell body Ω_S whose undeformed and deformed middle surfaces are denoted by $\bar{\Gamma}$ and Γ, respectively. The surface basis vectors corresponding to $\bar{\Gamma}$ and Γ are

$$\bar{\boldsymbol{a}}_\alpha=\bar{\boldsymbol{X}}(\xi^1,\xi^2)_{,\alpha},\qquad \boldsymbol{a}_\alpha=\boldsymbol{X}(\xi^1,\xi^2)_{,\alpha}, \tag{2.5}$$

respectively. Here and henceforth a comma is used to denote partial differentiation and Greek indices take the values 1 and 2. The local covariant basis vectors are defined as

$$\bar{\boldsymbol{g}}_\alpha=\bar{\boldsymbol{a}}_\alpha+\xi^3(\bar{\boldsymbol{a}}_3)_{,\alpha},\qquad \bar{\boldsymbol{g}}_3=\bar{\boldsymbol{a}}_3, \tag{2.6}$$

$$\boldsymbol{g}_\alpha=\boldsymbol{a}_\alpha+\xi^3(\eta\boldsymbol{a}_3)_{,\alpha},\qquad \boldsymbol{g}_3=\eta\boldsymbol{a}_3, \tag{2.7}$$

where ξ^3 is the thickness coordinate, η is the thickness stretch, $\bar{\boldsymbol{a}}_3$ and $\boldsymbol{a}_3$ are the unit normal vectors to the undeformed and deformed middle surfaces, respectively. Contravariant basis vectors $\bar{\boldsymbol{g}}^i$ and $\boldsymbol{g}^i$ are defined such that $\bar{\boldsymbol{g}}_i\cdot\bar{\boldsymbol{g}}^j=\delta_i^j$ and $\boldsymbol{g}_i\cdot\boldsymbol{g}^j=\delta_i^j$ where δ_i^j is the Kronecker delta. In term of the co- and contravariant basis vectors, the deformation gradient tensor $\mathbf{F}$ for the shell body may be expressed in the form [27]

$$\mathbf{F}=\frac{\partial\boldsymbol{X}}{\partial\bar{\boldsymbol{X}}}=\frac{\partial\boldsymbol{X}}{\partial\xi^i}\otimes\bar{\boldsymbol{g}}^i=\boldsymbol{g}_i\otimes\bar{\boldsymbol{g}}^i, \tag{2.8}$$

where here and henceforth lowercase Latin indices range from 1 to 3 and summation over repeated indices is implied. The right Cauchy-Green strain tensor is then given as

$$\mathbf{C}=\mathbf{F}^{\mathrm{T}}\mathbf{F}=g_{ij}\bar{\boldsymbol{g}}^i\otimes\bar{\boldsymbol{g}}^j, \tag{2.9}$$

where $g_{ij}=\boldsymbol{g}_i\cdot\boldsymbol{g}_j$ is the covariant metric tensor.

The total strain energy of the thin shell is

$$\int_{\Omega_S} W\mathrm{d}\bar{\Omega}_S+\int_{\Gamma} H\mathrm{d}\Gamma, \tag{2.10}$$

which includes the strain-energy functions W, per unit undeformed volume of $\bar{\Omega}$, and H, per unit area of Γ. For the incompressible hyperelastic material, such as biological membranes, the following neo-Hookean strain energy function is considered

$$W(\mathbf{C})=\frac{E}{6}(I_1^C-3), \tag{2.11}$$

where E is the Young's modulus, I_1^C is the first invariant of the right Cauchy-Green tensor $\mathbf{C}$. To model the red blood cell membrane, the strain energy function proposed by Skalak *et al.* [35] is used. In addition, the Helfrich [14] bending energy function for biological membranes is considered, given by

$$H=2\kappa_B(\kappa_m-\kappa_m^R)^2, \tag{2.12}$$

where κ_B is the scalar bending modulus, κ_m and κ_m^R are the mean curvature of the current and reference configurations, respectively.

The Kirchhoff stress tensor can be expressed as

$$\boldsymbol{\tau}=\tau^{ij}\boldsymbol{g}_i\otimes\boldsymbol{g}_j, \tag{2.13}$$

with the components $\tau^{ij}=2\partial W/\partial g_{ij}-p_s\boldsymbol{g}^i\cdot\boldsymbol{g}^j$, where p_s denotes the hydrostatic pressure which can be calculated from the plane stress assumption. The stress resultant $\boldsymbol{n}^i$, and the moment resultant $\boldsymbol{m}^\alpha$ are defined as

$$\boldsymbol{n}^i=\int_{-\bar{h}/2}^{\bar{h}/2}\boldsymbol{\tau}\cdot\boldsymbol{g}^i\bar{\nu}\mathrm{d}\xi^3, \tag{2.14}$$

$$\boldsymbol{m}^\alpha=\int_{-\bar{h}/2}^{\bar{h}/2}\boldsymbol{\tau}\cdot\boldsymbol{g}^\alpha\xi^3\bar{\nu}\mathrm{d}\xi^3, \tag{2.15}$$

where $\bar{\nu}$ accounts for the curvature of the shell in the volume integration [7, 34]. The bending stress follows from (2.12) by the work conjugacy, with the result

$$q^{\alpha\beta}=\frac{\partial H}{\partial\kappa_{\alpha\beta}}=2\kappa_B\left(\kappa_m-\kappa_m^R\right)g^{\alpha\beta}. \tag{2.16}$$

At equilibrium, the variation of the potential energy of the shell is zero, i.e.

$$\delta\Pi=\delta\Pi_{\text{int}}+\delta\Pi_{\text{ext}}=0, \tag{2.17}$$

where $\delta\Pi_{\text{ext}}$ is the variation of the potential energy of the external forces. The variation of the potential of the internal forces can be expressed as

$$\delta\Pi_{\text{int}}=\int_{\bar{\Omega}_S}\frac{\partial W}{\partial \mathbf{F}}:\delta\mathbf{F}\mathrm{d}\bar{\Omega}_S+\int_{\Gamma}\frac{\partial H}{\partial\kappa_{\alpha\beta}}\delta\kappa_{\alpha\beta}\mathrm{d}\Gamma. \tag{2.18}$$

Substituting Eqs. (2.8), (2.11) and (2.16) into (2.18) and a straightforward manipulation yields the following formulation

$$\int_{\bar{\Gamma}}\left[\boldsymbol{n}^{\alpha}\cdot\delta\boldsymbol{a}_{\alpha}+\eta\boldsymbol{n}^{3}\cdot\delta\boldsymbol{a}_{3}+\boldsymbol{m}^{\alpha}\cdot(\eta\delta\boldsymbol{a}_{3})_{,\alpha}\right]\mathrm{d}\bar{\Gamma}+\int_{\Gamma}q^{\alpha\beta}\left[\delta\boldsymbol{a}_{\alpha,\beta}\cdot\boldsymbol{a}_{3}+\boldsymbol{a}_{\alpha,\beta}\cdot\delta\boldsymbol{a}_{3}\right]\mathrm{d}\Gamma+\delta\Pi_{\text{ext}}=0. \tag{2.19}$$

Details for the derivation of Eq. (2.19) are given in [7,22].

3 Numerical method

3.1 Front-tracking method

To handle the coupling between the fluid and the capsule motion, a front-tracking method based on the immersed boundary method [28] is used. The immersed boundary method represents the surface by a control mesh containing a set of NP control points $\mathbf{x}_I, I=1,\cdots,\text{NP}$. The force per unit area $\boldsymbol{f}^s_I(\xi^1,\xi^2,t)$ is computed at these control points and is distributed to the Cartesian grid points using a discrete delta function $D_h(\boldsymbol{x})$ [28] as

$$\boldsymbol{f}(\boldsymbol{x},t)=\sum_{I=1}^{\text{NP}}\boldsymbol{f}^s_I(\xi^1,\xi^2,t)D_h(\boldsymbol{x}-\mathbf{x}_I(t))\triangle\xi^1\triangle\xi^2. \tag{3.1}$$

The force at node I can be derived by introducing the interpolated parametric

$$\mathbf{x}(\xi^1,\xi^2)=\sum_I N^I(\xi^1,\xi^2)\mathbf{x}_I, \tag{3.2}$$

where $N^I(\xi^1,\xi^2)$ is a basis function defined on the modified Loop's subdivision surfaces, into the weak form (2.19). This yields

$$\begin{aligned}\int_{\bar{\Gamma}}&\left[\boldsymbol{n}^{\alpha}\cdot\frac{\partial\boldsymbol{a}_{\alpha}}{\partial\mathbf{x}_I}+\eta\boldsymbol{n}^{3}\cdot\frac{\partial\boldsymbol{a}_3}{\partial\mathbf{x}_I}+\boldsymbol{m}^{\alpha}\cdot\left(\eta\frac{\partial\boldsymbol{a}_3}{\partial\mathbf{x}_I}\right)_{,\alpha}\right]\mathrm{d}\bar{\Gamma}\\&+\int_{\Gamma}q^{\alpha\beta}\left[\left(\frac{\partial\boldsymbol{a}_{\alpha}}{\partial\mathbf{x}_I}\right)_{,\beta}\cdot\boldsymbol{a}_3+\boldsymbol{a}_{\alpha,\beta}\cdot\frac{\partial\boldsymbol{a}_3}{\partial\mathbf{x}_I}\right]\mathrm{d}\Gamma+\int_{\Gamma}\boldsymbol{f}^sN^I\mathrm{d}\Gamma=0\end{aligned} \tag{3.3}$$

for $I=1,\cdots,\text{NP}$. For the shape functions defined in Section 3.2, the forces at node I can be approximated by averaging as

$$\boldsymbol{f}^s_I=\frac{\int_{\Gamma}\boldsymbol{f}^sN^I\mathrm{d}\Gamma}{\int_{\Gamma}N^I\mathrm{d}\Gamma}. \tag{3.4}$$

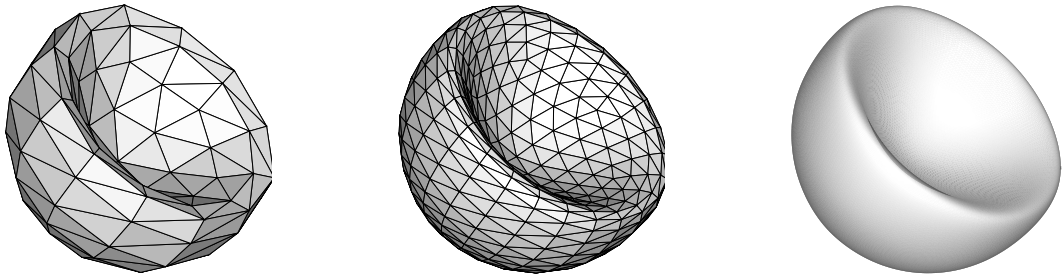

Figure 1: Subdivision using the Loop scheme: control mesh, first subdivided mesh and the limit surface.

Eq. (3.3) leads to

$$\boldsymbol{f}_I^s = -\frac{\boldsymbol{f}_I^{\text{int}}}{\int_\Gamma N^I \mathrm{d}\Gamma}, \tag{3.5}$$

where $\boldsymbol{f}_I^{\text{int}}$ is the internal force at node I and follows in the form

$$\begin{aligned}\boldsymbol{f}_I^{\text{int}} = &\int_{\bar{\Gamma}} \left[\boldsymbol{n}^\alpha \cdot \frac{\partial \boldsymbol{a}_\alpha}{\partial \mathbf{x}_I} + \eta \boldsymbol{n}^3 \cdot \frac{\partial \boldsymbol{a}_3}{\partial \mathbf{x}_I} + \boldsymbol{m}^\alpha \cdot \left(\eta \frac{\partial \boldsymbol{a}_3}{\partial \mathbf{x}_I} \right)_{,\alpha} \right] \mathrm{d}\bar{\Gamma} \\ &+ \int_\Gamma q^{\alpha\beta} \left[\left(\frac{\partial \boldsymbol{a}_\alpha}{\partial \mathbf{x}_I} \right)_{,\beta} \cdot \boldsymbol{a}_3 + \boldsymbol{a}_{\alpha,\beta} \cdot \frac{\partial \boldsymbol{a}_3}{\partial \mathbf{x}_I} \right] \mathrm{d}\Gamma. \end{aligned} \tag{3.6}$$

Once the force density is computed and distributed to the Cartesian grid, the Navier-Stokes equations are solved for the pressure and velocity fields. The velocity field is then used to advance the position of the immersed boundary in an implicit manner [21].

3.2 Surface discretization with modified Loop's subdivision scheme

Le [21] has recently employed the C^1-interpolation scheme based on the Loop's subdivision surfaces proposed in [7,8] for studying the deformation of elastic capsule in fluid flow. The main idea behind the Loop's subdivision surfaces [26] is to represent a smooth surface by a triangular control-mesh. Subdivision algorithms recursively refine this control mesh by adding new vertices, edges and faces to produce a sequence of finer meshes that converge to a smooth limit surface that is topologically equivalent to the original control mesh. This process is illustrated in Fig. 1. For the sake of completeness, the original and modified Loop's algorithms and the surface parameterization are described in this section.

In a refinement step, each triangle is split into four, and the nodal positions of the refined mesh are calculated as weighted averages of the nodal positions of the coarser mesh and given in the form of subdivision masks. Subdivision masks are classified into vertex masks and edge masks as depicted in Fig. 2. The weights used in the vertex mask are $\alpha = (\frac{3}{8} + \frac{1}{4}\cos\frac{2\pi}{n})^2 + \frac{3}{8}$ and $\beta = \frac{1}{n}(1-\alpha)$, where n is the valence of the vertex. The edge

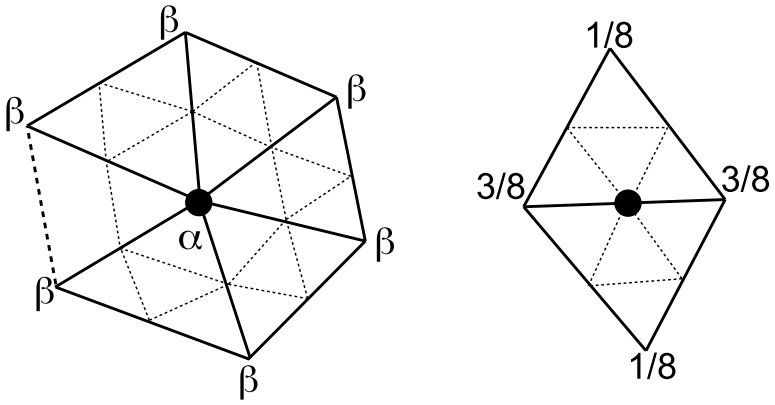

Figure 2: Vertex mask and edge mask used in Loop's algorithm.

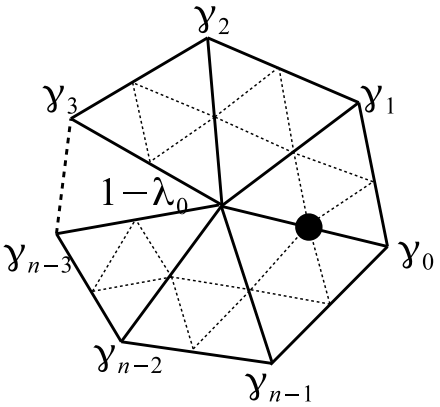

Figure 3: Modified edge mask used in the modified Loop's algorithm.

mask assigns weights to the vertices of the two triangles that share the edge and do not depend on the valence. The vertex masks of the modified Loop's algorithm [25] are similar to those of Loop's scheme except that the values of the weights α,β are different. The edge mask of the modified Loop's algorithm has larger support and is depicted in Fig. 3. This edge mask is applied for an edge with extraordinary incident vertex ($n\neq 6$). The modified edge mask returns to the original edge mask if both incident vertices are ordinary. The sum of the mask weights $1-\lambda_0,\gamma_0,\cdots,\gamma_{n-1}$ is equal to 1, so $\lambda_0=\sum\gamma_i$. The mask weights for arbitrary $n\geq 6$ have been proposed in [25]:

$$\gamma_i=\frac{2\lambda_1^3}{n(1-\lambda_1)}(1+u_i)\left(u_i+\frac{1}{\lambda_1}-\frac{3}{2}\right)^2, \tag{3.7}$$

where $\lambda_1=\frac{3}{8}+\frac{1}{4}\cos\frac{2\pi}{n}$ and $u_i=\cos\frac{2\pi i}{n}, i=0,\cdots,n-1$. For the cases where $n=3,4$ and 5, the

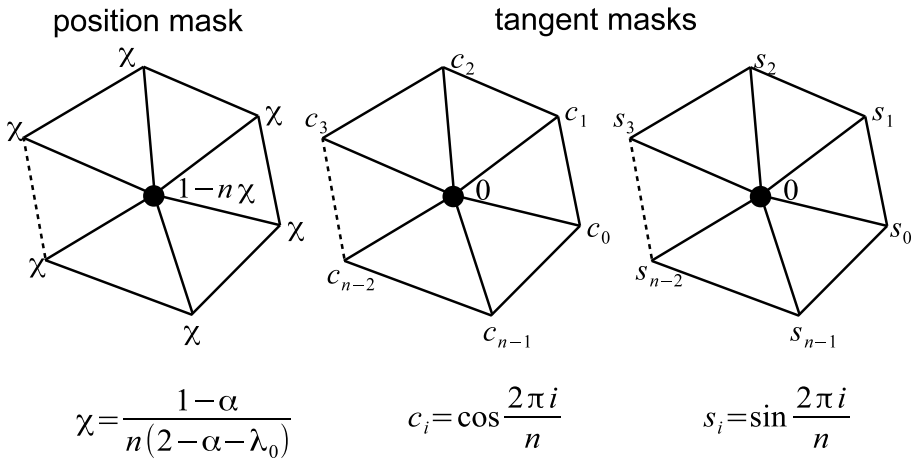

Figure 4: Limit masks for the modified Loop's algorithm.

mask weights are given as

$$\gamma_i=\begin{cases}\frac{1}{6}\left(\frac{5}{4}+u_i\right), & n=3,\\ \frac{1}{2}\left(\frac{1}{2}+\frac{3}{8}u_i\right)^2, & n=4,\\ \frac{3+\sqrt{5}}{32}\left(1-\frac{1}{\sqrt{5}}+u_i\right)^2, & n=5.\end{cases} \tag{3.8}$$

By construction, it is known that $\lambda_0=\sum_{i=0}^{n-1}\gamma_i$, hence the central weight for the edge mask is $1-\lambda_0$. The central weight for the vertex mask is found by

$$\alpha=1-\lambda_0+\lambda_1^2. \tag{3.9}$$

To compute the limiting positions of the nodes, the position mask as shown in Fig. 4 can be used. Similarly, the two tangent vectors (and from them the surface normal) to the limit surface can be computed using the tangent masks.

For numerical evaluation of stress and moment resultants in thin-shell analysis, a parameterization of the surface and the ability to evaluate surface derivatives at arbitrary parameter locations are needed. For a regular triangle, all of whose nodes have six neighbors, the Loop subdivision surface reduces to the common box splines (shown schematically in Fig. 5) for which analytical expressions are available. Each node of the regular triangle has exactly six neighbors and the total number of nodes in the triangle or adjacent to it is 12. Therefore, the local parameterization of the limit surface can be expressed in terms of box-spline basis functions as

$$\mathbf{x}(\xi^1,\xi^2)=\sum_{I=1}^{12}N^I(\xi^1,\xi^2)\mathbf{x}_I=\mathbf{X}^T\mathbf{N}(\xi^1,\xi^2), \tag{3.10}$$

where $\mathbf{X}$ is a 12×3 matrix containing the control vertices of the patch ordered as in Fig. 5 and $\mathbf{N}(\xi^1,\xi^2)$ is the vector of basis function $N^I(\xi^1,\xi^2)$. The precise form of the basis functions $N^I(\xi^1,\xi^2)$ can be found in [37].

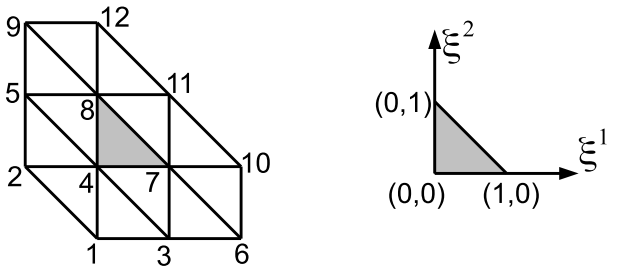

Figure 5: A regular common box spline patch defined by 12 control vertices.

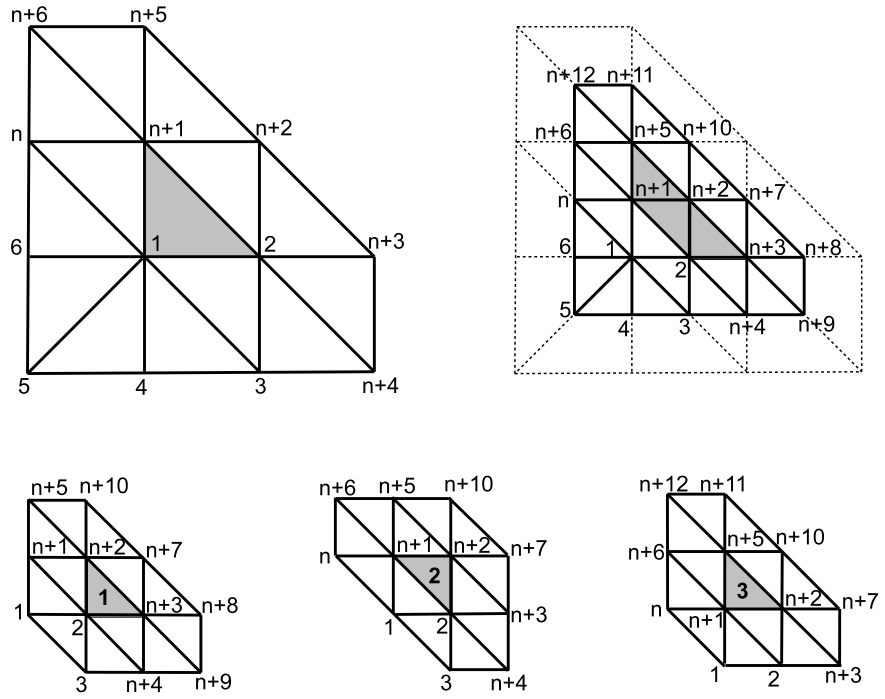

Figure 6: An irregular patch defined by 13 control vertices. After one subdivision step, three-quarters of the triangular patch become regular and can be evaluated.

For irregular triangles, the local parameterization of the Loop's subdivision surface was proposed by Stam [37] based on the eigen-decomposition of the refinement matrix. Stam's method described a very effective way to evaluate surface properties at an arbitrary location on the limit surface without performing a large number of refinements. A simplified form of Stam's method is used and the parameterization of the modified Loop surfaces for irregular triangles is described. For simplicity, it is assumed that irregular patches have one extraordinary vertex only including the vertices labelled from "n+2" to "n+6" as shown on the top left of Fig. 6. This assumption can always be met for arbitrary initial meshes through at most two steps of subdivision, which has the effect of separating extraordinary vertices. The triangular patch associated with the shaded element in

this figure is defined by $n+6$ vertices where n is the valence of the extraordinary vertex labelled "1" in the middle of the figure. The control vertices are stored in a $(n+6)\times 3$ matrix

$$\mathbf{X}_0^T = (\mathbf{x}_{0,1}, \cdots, \mathbf{x}_{0,n+6}).$$

After one subdivision step, a new set of $n+12$ vertices

$$\bar{\mathbf{X}}_1^T = (\mathbf{x}_{1,1}, \cdots, \mathbf{x}_{1,n+12})$$

are generated as shown on the top right of Fig. 6. The vertices $\bar{\mathbf{X}}_1$ can be obtained as following

$$\bar{\mathbf{X}}_1 = \bar{\mathbf{A}}\mathbf{X}_0, \tag{3.11}$$

where

$$\bar{\mathbf{A}} = \begin{pmatrix} \mathbf{S} & \mathbf{0} \\ \mathbf{S_{11}} & \mathbf{S_{12}} \\ \mathbf{S_{21}} & \mathbf{S_{22}} \end{pmatrix}$$

and the blocks are defined in Appendix A. It is noticed that three-quarters of the triangular patch become regular and can be evaluated. To calculate the integrations in Eq. (3.6), one-point quadrature rule with the quadrature point located at the barycenter $(\xi^1 = 1/3, \xi^2 = 1/3)$ of the triangular element is used. After one subdivision step, the quadrature point lies within the second regular sub-patch as illustrated in Fig. 6. And this second regular sub-patch labelled "2" in Fig. 6 (bottom middle) can be used to evaluate the function values at the quadrature point. The control vertices of the sub-patch 2 are $\mathbf{P}\bar{\mathbf{X}}_1$ where $\mathbf{P}$ is a $12\times(n+12)$ "picking matrix" whose each row is filled with zeros except for a one in the column corresponding to the index of sub-patch 2 [37]. It should be noted that the coordinates of the quadrature point need to be transformed in the regular sub-patches. In sub-patch 2, the new local coordinates of the quadrature point are $\tilde{\xi}^1 = 1-2\xi^1$ and $\tilde{\xi}^2 = 1-2\xi^2$. The function values for sub-patch 2 can now be evaluated using the interpolation rule

$$\mathbf{x}(\xi^1, \xi^2) = (\mathbf{P}\bar{\mathbf{A}}\mathbf{X}_0)^T \mathbf{N}(\tilde{\xi}^1, \tilde{\xi}^2). \tag{3.12}$$

It should be noted that the main different between the original and modified Loop's schemes is the parameterization of the surface at irregular elements where the subdivision matrix $\bar{\mathbf{A}}$ is modified to satisfy the bounded curvature constraints. Since the number of irregular elements is just a small portion of the total number of elements of the surface mesh, the modified Loop's scheme may improve the stability of the numerical method slightly. But it definitely improves the robustness of the subdivision thin-shell model.

4 Results

In this section, the deformation and interaction of elastic capsules of radius a in shear flow given by the velocity $\boldsymbol{u} = (\dot{\gamma}y, 0, 0)$ is investigated, where $\dot{\gamma}$ is the shear rate. The

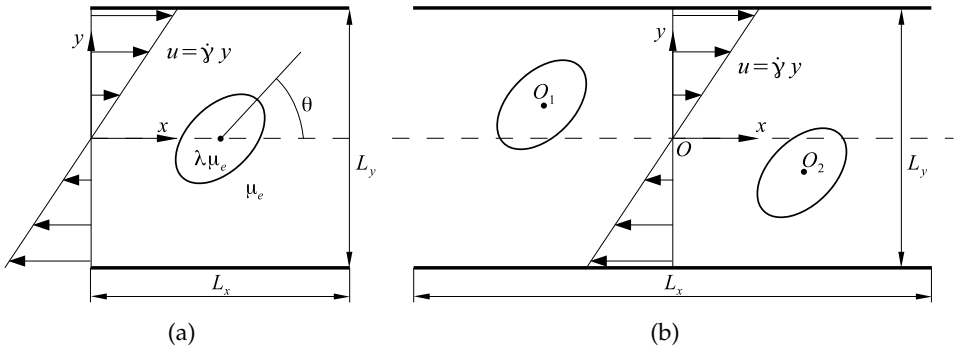

Figure 7: System definition of (a) a single capsule and (b) a pair of capsules in bounded shear flow.

capsules' motion and deformation depend on the initial position, dimensionless shear rate $G=\mu\dot{\gamma}a/(E\bar{h})$, bending modulus $\hat{\kappa}_B=\kappa_B/(a^2E\bar{h})$, viscosity ratio, λ and Reynolds number $Re=\rho\dot{\gamma}a^2/\mu$. Here, the Reynolds number is chosen to be sufficiently small so that the inertia effect is neglected. Simulations are performed on a computational domain of size $L_x\times L_y\times L_z$ with Dirichlet boundary condition for the velocity at $y=\pm L_y/2$ and periodic at other boundaries. The initial capsule shape is taken to be a reference state for both in-plane tensions and bending moments. The deformation of the capsules is described by the Taylor shape parameter D_{xy} and inclination angle θ [32]. The geometry of the system for a single capsule and a pair of capsules are shown in Fig. 7.

4.1 Single capsule in shear flow

The present method is validated by studying the convergence of the deformation of a spherical neo-Hookean capsule for $G=0.1$, $\lambda=2$ and $\hat{\kappa}_B=0.01$ at $Re=0.01$. In a computational domain of size $L_x=L_y=L_z=10a$, grid refinement study is performed for four different fluid grids, i.e $64\times64\times64$, $96\times96\times96$, $128\times128\times128$ and $192\times192\times192$ grids with the corresponding surface meshes of 5120, 8192, 20480 and 32768 triangular elements, respectively. The deformation parameter, D_{xy}, and inclination angle, θ, at different mesh resolutions are shown in Fig. 8. It can be seen that the results converge with increasing mesh resolution and the $128\times128\times128$ Cartesian grid with surface mesh of 20480 elements is sufficient to capture accurately the deformation parameters of the capsule. Fig. 9 shows the results for D_{xy} and θ, with $\lambda=1$ and $\hat{\kappa}_B=0$ at different dimensionless shear rates G. The results are compared with those obtained using the quadratic triangular elements [22] and good agreement is observed in Fig. 9. It is noted that the deformation parameter and the inclination angle obtained in [22] have been validated against those in [2, 32, 38] and the present results are almost identical to those obtained by the original Loop's scheme [21]. The modified Loop's scheme does not have noticeable advantages over the original one since we do not see large mesh distortion in the simulations of single capsule. The results also show that the spherical capsule deforms

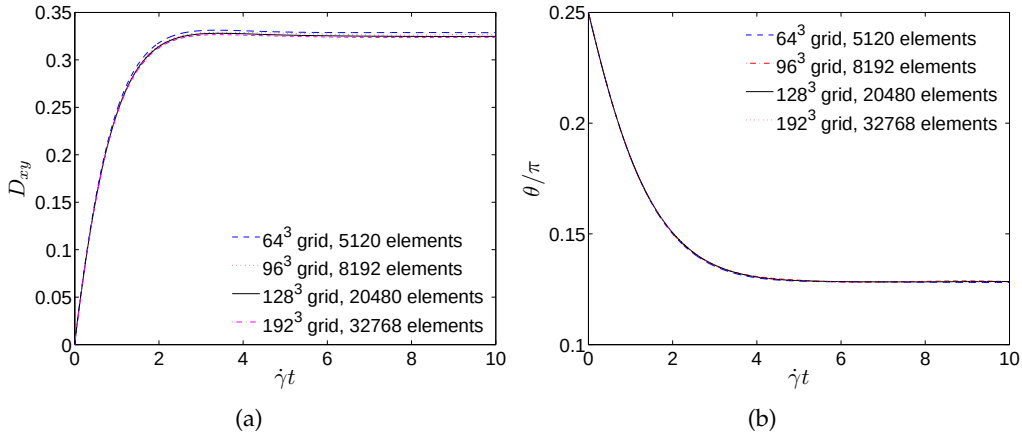

Figure 8: Grid refinement study of (a) the deformation parameter and (b) inclination angle for spherical capsule with $\lambda=2$, $G=0.1$ and $\hat{\kappa}_B=0.01$.

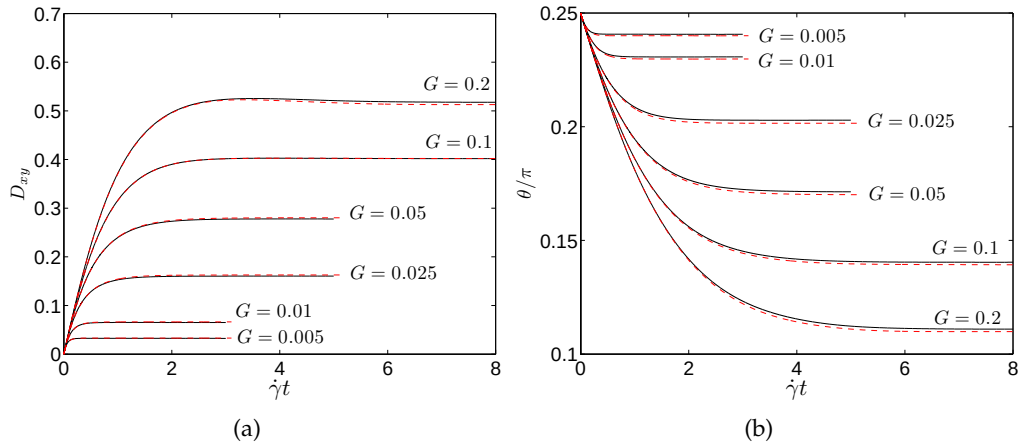

Figure 9: The evolution of (a) the deformation parameter and (b) inclination angle for spherical capsule with $\lambda=1$ and $\hat{\kappa}_B=0$ at different G. The solid lines are the results obtained with modified Loop subdivision elements and the dashed lines are obtained with the quadratic triangular elements [22].

to an ellipsoidal shape and the capsule membrane rotates in a tank-treading mode [32]. The tank-treading mode only results in a crossing motion when two spherical capsules interact with each other in infinite shear flow as can be seen later.

Next simulations for the biconcave capsules with Skalak's strain energy function for red-blood cell membrane are performed. The mapping for the biconcave disk shape assumed by red blood cells at rest is given in [22]. The modified Loop's scheme is able to reproduce the tumbling and swinging motions of the biconcave capsules at different shear rates and viscosity ratios. In addition it can capture the transition dynamics between tumbling and swinging motions. A phase diagram of a biconcave capsule with different motion modes as a function of the viscosity ratio λ and the inverse dimensionless shear

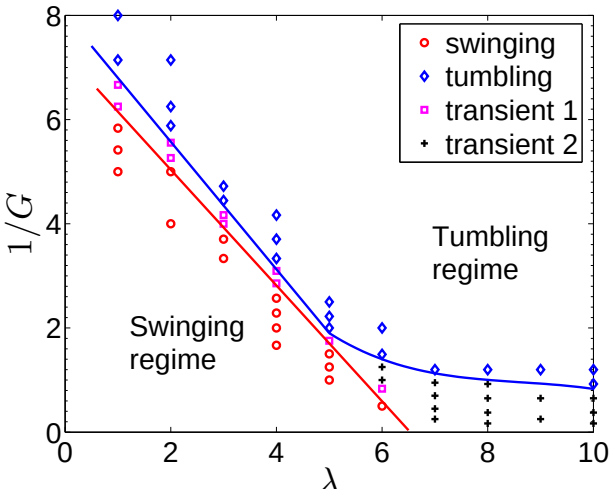

Figure 10: Phase diagram of a biconcave capsule with swinging and tumbling regimes as a function of λ and $1/G$ at $\hat{\kappa}_B = 0.01$.

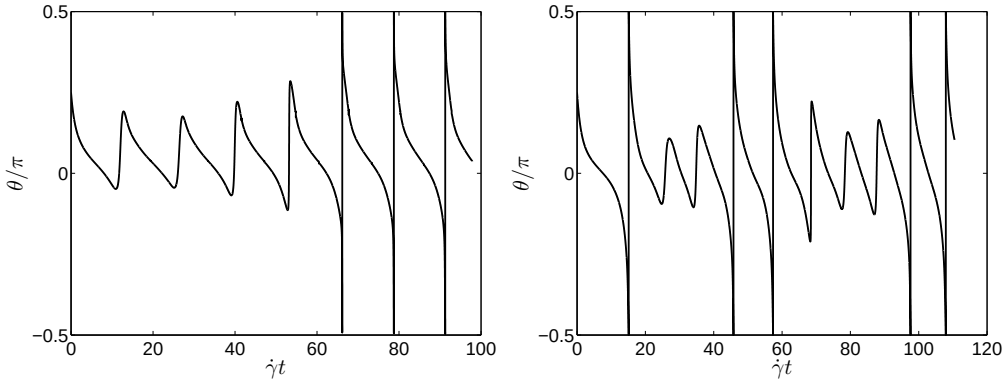

Figure 11: Transient motions of biconcave capsules: (a) swinging to tumbling at $\lambda = 2$, $G = 0.2$ and (b) intermittent tumbling to swinging at $\lambda = 7$, $G = 1.4$.

rate $1/G$ is shown in Fig. 10. The phase diagram is obtained at constant reduced bending modulus $\hat{\kappa}_B = 0.01$, which is on the order of bending stiffness of healthy red-blood cell [29]. At high dimensionless shear rate G and low viscosity ratio λ, the swinging motion is observed. At low dimensionless shear rate and high viscosity ratio, the capsule undergoes tumbling motion because the fluid shear stress acting on the membrane is no longer sufficient to force the membrane to tank tread. The transition dynamics from swinging to tumbling at low viscosity ratio (Fig. 11(a)) is also observed. At a narrow range of high viscosity ratio and high dimensionless shear rate, an intermittent regime of successive tumbling and swinging can be seen as shown in Fig. 11(b).

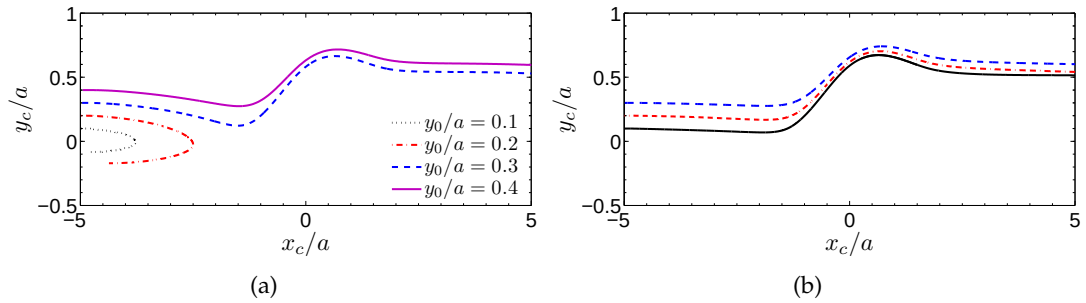

Figure 12: Trajectories of the spherical capsule center O_1 with different initial locations y_0/a in shear flow in a channel of height (a) $L_y/a=10$ and (b) $L_y/a=30$.

4.2 Hydrodynamic interaction between two identical capsules

The motion of an individual capsule will affect the hydrodynamic interaction between them. In this section the hydrodynamic interaction between two identical capsules in bounded shear flow is investigated. The computational domain is chosen as: $L_x=20a$, $L_z=10a$ and L_y is varied to study the effects of the channel height on the interaction. The mesh sizes are the same as those used for single capsule. The capsules with centers of mass O_1 and O_2 are initially located in the same shear plane at $(-x_0,y_0,0)$ and $(x_0,-y_0,0)$, respectively as shown in Fig. 7(b).

4.2.1 Interaction of spherical capsules

First the hydrodynamic interaction between two neo-Hookean spherical capsules is investigated. Fig. 12 shows the trajectories of the capsule center of mass O_1, $(x_c,y_c,0)$, with different initial vertical separations y_0/a for two channel heights of $L_y/a=10$ and $L_y/a=30$. Here $\lambda=1$, $G=0.2$, $\hat{\kappa}_B=0.01$, $Re=0.001$ and $x_0/a=5$ are considered. For sufficiently large initial vertical offsets Δy_0 the trajectories of the spherical capsules in wall-bounded shear flow are qualitative similar to those in free space ($L_y/a\geq 30$). Due the relative velocity between the two capsules, they approach each other and subsequently cross over each other. After crossing the vertical separation decreases and maintains a constant value as they move away from each other. This type of interaction has also been observed in [10, 19] and is referred to as a crossing motion. The only distinctive feature of the trajectory depicted in Fig. 12(a) is that y_c decreases before reaching the maximum when the capsules roll over each other (i.e. $\Delta x_c\approx 0$), while in free space y_c would increase monotonically. For smaller initial vertical offsets Δy_0 the capsules in wall-bounded shear flow ($L_y/a=10$) approach each other due to the non-zero relative velocity between them but they do not cross over each other upon encounter. Instead, they reverse their directions of motion when their centers of mass cross the $y=0$ axis as seen in Fig. 12(a) for $y_0/a=0.1$, 0.2. The reversing motion can be explained by examining the streamlines around a single capsule in tank-treading mode as illustrated in Fig. 13. Fig. 13(a) shows fluid streamlines around a capsule in the middle of the channel with wall sepa-

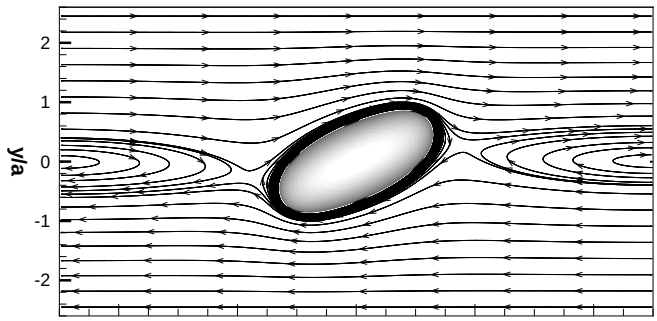

(a) $L_y/a=5$

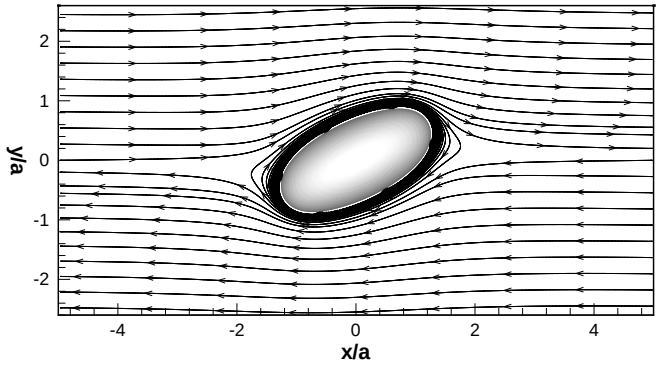

(b) $L_y/a=30$

Figure 13: Streamlines around a single capsule in a channel with (a) $L_y/a=5$ and (b) $L_y/a=30$.

ration $L_y/a=5$. As expected, in a wall-bounded system there is a region of reversing streamlines. If the center of mass of another capsule falls within this reversing region, the capsule will change its direction of motion and result in a reversing type of interaction. Fig. 13(b) shows the familiar streamlines around a capsule in the channel with wall separation $L_y/a=30$ which is large enough to represent the unbounded shear flow. It should be noted that the region of reversing streamlines becomes smaller with increasing channel wall separation L_y/a and disappears in unbounded shear flow. This is further illustrated in Fig. 14, where the trajectory-bifurcation point y_0^c separating reversing and crossing trajectories with L_y/a at $G=0.1$, 0.2 and 0.5 is plotted. It can be seen that the width in y of the reversing zone at a given wall separation L_y/a decreases with increasing G. This is because of the larger deformation and greater alignment of the capsule with the undisturbed flow at larger dimensionless shear rate G.

4.2.2 Interaction of biconcave capsules

Now the interaction between two biconcave capsules with Skalak's strain energy function for red blood cell membrane is considered. The capsules are initially inclined at an

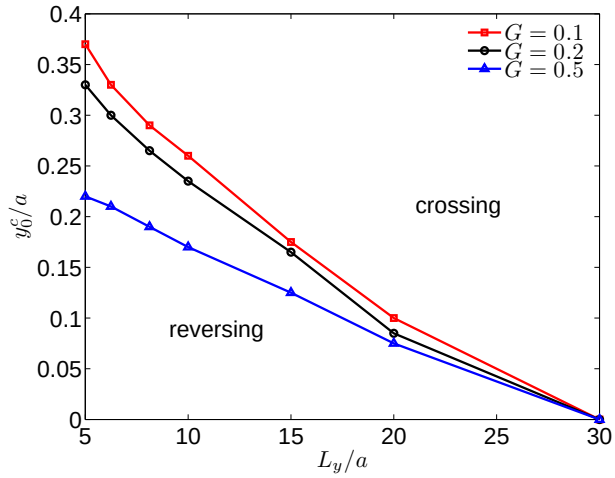

Figure 14: The trajectory-bifurcation point y_0^c separating reversing and crossing trajectories with L_y/a for spherical capsules.

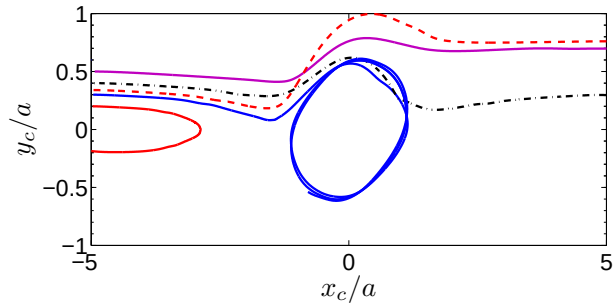

Figure 15: Trajectories of the biconcave capsule center O_1 with $L_y/a=10$, $G=0.05$ at different initial positions.

angle $\theta_0=\pi/4$ with respect to the streamlines of the undisturbed flow. Fig. 15 shows several trajectories of the biconcave capsule O_1 corresponding to various types of interaction such as reversing, crossing and continuous rotation. The trajectories of biconcave capsules are studied for $G=0.05$, $\hat{\kappa}_B=0.01$, $Re=0.001$, $L_y/a=10$, $x_0/a=-5$ at different initial offsets Δy_0. It is noted that at this shear rate, the capsules exhibit tumbling motion. At $y_0/a=0.2$, the capsules exhibit the reversing motion due to the wall-bounded effect as explained previously for two spherical capsules. The reversing zone can be seen clearly in Fig. 16 where the streamlines around a single biconcave capsule undergoing tumbling motion are plotted. In contrast to the streamlines around a spherical capsule, a large recirculation zone in the middle of the domain and around the biconcave capsule can be seen. At some points in time during the tumbling motion of the capsules the recirculation zone may be large enough to trap another capsule inside and leads to the continuous rotation. The trajectory of capsule O_1 corresponding to the continuous rotation is shown in Fig. 15 for $y_0/a=0.3$. At larger initial vertical separation the two capsules approach each other and subsequently cross over each other. Fig. 17 shows the trajectory-bifurcation point y_0^c

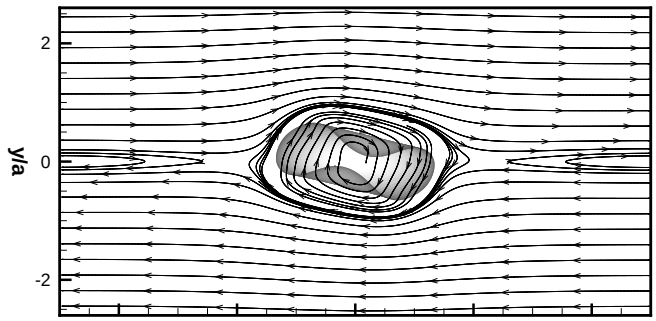

(a) $\dot{\gamma}t=6$

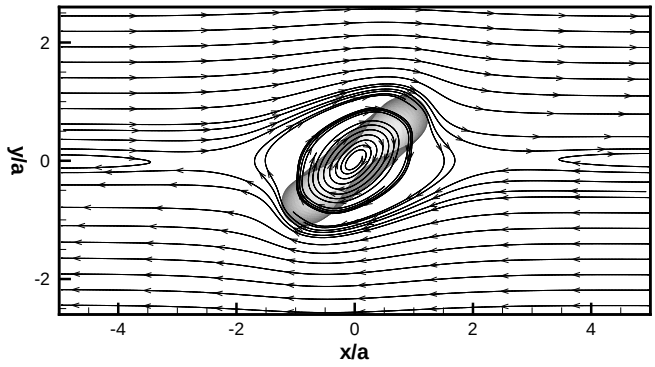

(b) $\dot{\gamma}t=7$

Figure 16: Streamlines around a single biconcave capsule in a channel with $L_y/a=10$ at different times: (a) $\dot{\gamma}t=6$ and (b) $\dot{\gamma}t=7$.

separating the reversing motion and other types of interaction with L_y/a at $G=0.2, 0.05$. It should be noted that at $G=0.2$ each biconcave capsule undergoes swinging motion and therefore only exhibits reversing and crossing types of interaction. The continuous rotation only occur when the individual capsule undergoes tumbling motion at small dimensionless shear rate. The reversing, crossing and continuous rotation motions have been observed in previous studies [3, 11, 19]. In the present study, we observe new types of complicated crossing behaviors which could decrease or increase the vertical trajectory shifts.

As shown in Fig. 12(b) the hydrodynamic interactions of the spherical capsules during the crossing lead to irreversible trajectory shifts. The trajectory shifts are positive, meaning that the crossing results in shear-induced diffusion. The similar simple crossing behavior for biconcave capsules undergoing swinging motion at high dimensionless shear rates is seen. However, when each biconcave capsule undergoes tumbling motion while crossing each other, the crossing becomes complicated. For example, Fig. 15 shows that the crossing interaction between two capsules when the initial separation $y_0/a=0.4$ (dash-dotted line) results in a negative cross-flow displacement. After passing the center

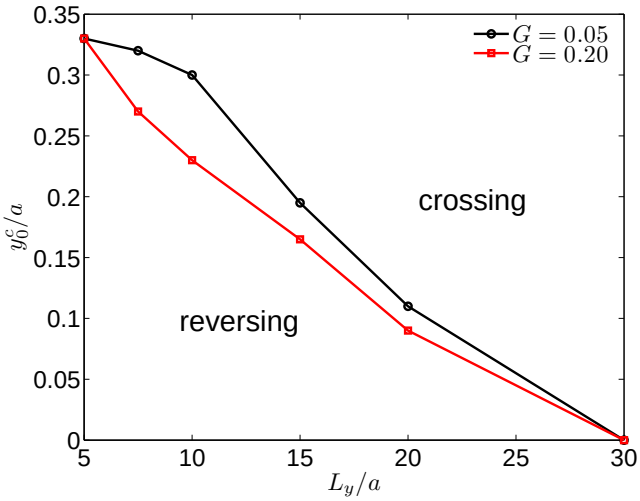

Figure 17: The trajectory-bifurcation point y_0^c separating reversing and crossing trajectories with L_y/a for biconcave capsules.

plane $x = 0$, the capsules follow the path of the continuous rotation trajectories but the positive pressure in the gap between the two capsules move them apart and prevent a full continuous rotation motion. Consequently, the final trajectory shift is either null or negative. When the initial separation is $y_0/a = 0.34$ (dash line), the crossing interaction between the two capsules results in a large final trajectory shift. The final vertical position is even larger than that of the capsule with greater initial separation such as $y_0/a = 0.5$. We do not see this behavior for spherical capsules where the final vertical position increases monotonically with the initial vertical position [19]. The jump in the value of the trajectory shift is due to a head-on collision of the two capsules under tumbling motion as illustrated in Fig. 18. Fig. 18 shows the snapshots of the biconcave capsules at different times during the head-on collision. At $\dot{\gamma}t = 13$, the two capsules approach each other while undergo tumbling motion. The capsule on the left rotates downward while the one on the right rotates upward. If each capsule undergoes swinging motion they may just slide over each other. However, due to the tumbling motion the capsules continue to rotate until they hit each other at $\dot{\gamma}t = 15$ and start to deform substantially at one side of each capsule at $\dot{\gamma}t = 17$ to 19. During this period, instead of tumbling around its center of mass, each capsules rotates around the center of the domain where the two capsules meet. Subsequently, the capsules separate and recover the biconcave shape as observed in Fig. 18(e) and Fig. 18(f). The head-on collision increases the hydrodynamic diffusion of a suspension of capsules since it increases the vertical shift. However, in a suspension, capsules approach each other from different shear planes with different orientations. So it is not very clear how the head-on collision or other types of interaction affect the diffusion of capsules in the suspension. Owing to the influence of the hydrodynamic interaction between capsules, a sufficiently large number of capsules must be used in simulations to adequately describe the bulk or macroscopic rheological properties of the suspension.

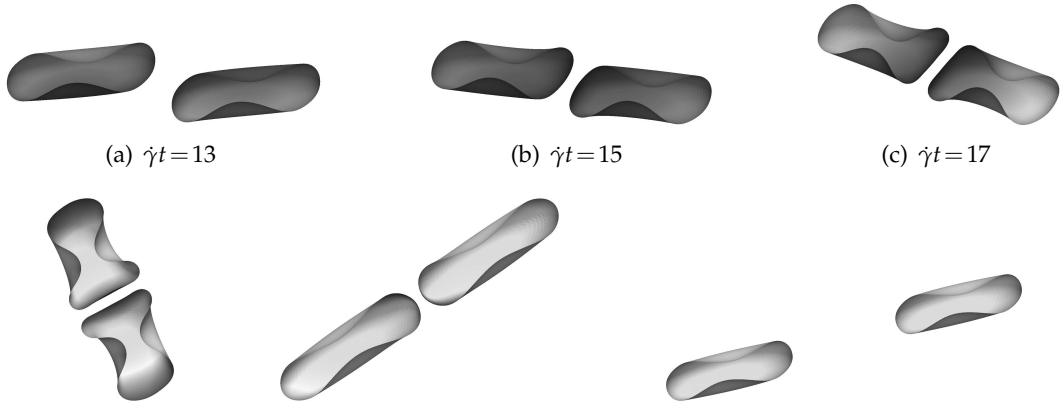

(a) $\dot{\gamma}t=13$ (b) $\dot{\gamma}t=15$ (c) $\dot{\gamma}t=17$

(d) $\dot{\gamma}t=19$ (e) $\dot{\gamma}t=21$ (f) $\dot{\gamma}t=23$

Figure 18: Shapes of the biconcave capsules during the head-on collision.

4.3 Hydrodynamic diffusion of a suspension of capsules

The complicated hydrodynamic interaction between two capsules affects the rheological properties of the suspension of capsules such as relative viscosity and hydrodynamic diffusion coefficient. Hydrodynamic or shear-induced diffusion of capsules in a suspension is the random walk motion away from the undisturbed trajectories of the capsules due to the interaction of the capsules with their neighbors. In this section, the hydrodynamic diffusion of a suspension of biconcave capsules in shear flow is studied to show that the modified Loop's subdivision scheme has improved the stability in the simulation over a long period of time. The simulations are performed for biconcave capsules which have random starting positions and are non-overlapping in a fluid domain as shown in Fig. 19. In these simulations, z is the direction of shear gradient and the parameters are chosen as $G=0.1$, $\hat{\kappa}_B=0.01$, $Re=0.001$ and $\lambda=1$.

The dimensionless variance of the displacement of the capsules in both the y- and z-directions is measured. The variance in the y-direction at the dimensionless time $\dot{\gamma}t$ is defined as

$$\sigma_y^2=\left(\left\langle(\Delta y)^2\right\rangle-\left\langle\Delta y\right\rangle^2\right)/a^2, \tag{4.1}$$

where Δy is the displacement of a capsule in the y-direction measured from a reference time and $\langle\ \rangle$ denotes averaging over all capsules in the computational domain at an instance in time. The reference time is set to be 10 dimensionless time units after the start of the simulation, which is about the time required for the capsules' deformation to reach their average values. The variance in the z-direction is defined in a similar manner. To determine the type of motion of the suspension (subdiffusion, diffusion or superdiffusion), $\sigma_i^2\propto t^{\alpha_i}$ is assumed, where $i=y$, z and calculate α_i by a least squares fit to the data. The variances for $t\in[100,1000]$ is used to calculate α_y and α_z as shown in Fig. 20. The initial motion is ballistic with $\alpha_i=2$ up to $\dot{\gamma}t\approx1$. The motion of the suspension eventually

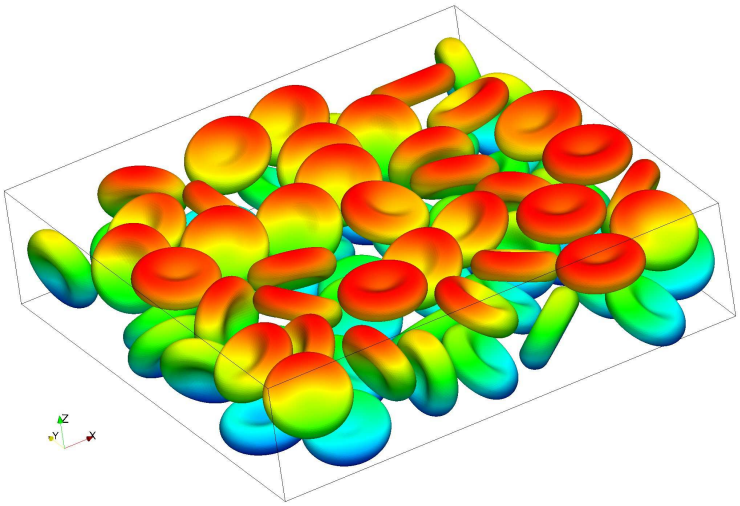

Figure 19: The fluid domain with dimensions $L_x = L_y = 16a$, $L_z = 4a$, enclosing 74 red blood cells leading to a volume fraction of 30%.

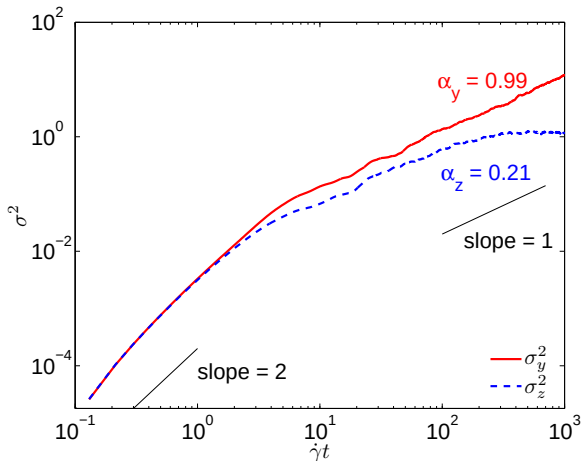

Figure 20: Variances of dimensionless displacement σ_y^2 and σ_z^2 vs. dimensionless time $\dot{\gamma}t$.

becomes diffusive in y-direction with $\alpha_y \approx 1$ and the diffusion coefficient $D_{yy} = 0.006$. The value of α_z shows that the motion in the z-direction is always subdiffusive with $\alpha_z \approx 0.21$ due to the hindrance of the walls. If one calculate α_z using the dimensionless variance data for $\dot{\gamma}t > 500$, $\alpha_z = 0$ will be obtained. That means the variance of the displacement of the capsules in the z-direction needs a long period of time to reach a constant value. Therefore a robust method is needed to carry out the simulations over a long time to get meaningful results. And to the best of our knowledge, the present method with modified Loop's subdivision scheme is the first method that has performed simulations for a dense suspension of biconcave capsules for $\dot{\gamma}t$ up to 1000. If the original Loop's scheme

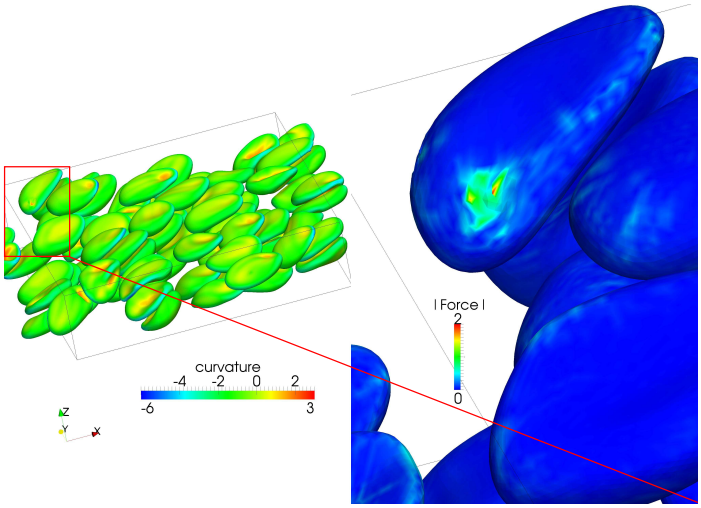

Figure 21: Snapshot showing the deformation of elastic capsules at time $\dot{\gamma}t=110$ for $G=0.1$, $\hat{\kappa}_B=0.01$ and $\lambda=1$ in a channel with volume fraction of 30%. The mean curvature on the capsule membranes is shown on the left and the force is shown on the right.

is used for the same simulation, the simulation can only be run for up to $\dot{\gamma}t\approx 110$ which is not long enough to capture the hydrodynamic diffusion of the suspension of capsules correctly. The original Loop's scheme suffers from the numerical instability due to the large errors in the calculated curvature and membrane force at the quadrature points in the irregular elements when the distortion of the membrane mesh is large enough. We note that the original Loop's scheme can produce an artifact of divergent curvature due to the lack of the bounded curvature constraints [25]. Fig. 21 shows a snapshot of the suspension of capsules at $\dot{\gamma}t=110$ before the numerical instability stops the simulation from running further. The mean curvature is shown on the left and the force magnitude is shown on the right of Fig. 21. The large error in the membrane force at the large distorted part of the membrane mesh leads to the numerical instability.

5 Conclusions

In this article, a thin-shell model with modified Loop's subdivision surfaces for describing the geometry of the capsule membrane and computing smooth force fields in the framework of the principle of virtual displacements is presented. The limit surface obtained by the modified Loop's algorithm obeys the bounded curvature constraints and can be described locally by the common box splines. The present method has been validated by studying the deformation of spherical capsules in shear flow. For a single biconcave capsule, a phase diagram is produced for systematic exploration of the biconcave capsule dynamics with swinging, tumbling and transient regimes as a function of viscosity ratio and dimensionless shear rate.

In bounded shear flow the hydrodynamic interaction between two spherical capsules results in the reversing or crossing trajectories depending on the initial vertical separation between the capsules. The trajectory-bifurcation plot for separating the reversing and crossing types of interaction for both spherical and biconcave capsules is obtained. For biconcave capsules, other interaction types such as rotation and head-on collision can be seen. The head-on collision is a special case of the crossing motion and results in a large trajectory shift which contribute to and enhance the hydrodynamic self-diffusivity in dilute suspensions.

The hydrodynamic diffusion of a suspension of capsules in bounded shear flow is also studied and the type of motion of the suspension is determined. The motion of the suspension is diffusive in the y-direction (or vorticity direction) and subdiffusive in the z-direction due to the hindrance of the walls. The numerical simulations also showed the ability of the modified Loop's subdivision scheme to improve the stability of the numerical method when there is a need to run simulation for a long period of time.

6 Acknowledgments

The second author is partially supported by the NSFC (91230108, 11101446), the PSTNS of Zhu Jiang in Guangzhou city (2011J2200099), Guangdong Natural Science Foundation (S2013010012250), the Fundamental Research Funds for the Central Universities (13lgzd07), the Specialized Research Fund for the Doctoral Program of Higher Education (20110171120048), Guangdong Provincial Government of China through the "Computational Science Innovative Research Team" program, and Guangdong Province Key Laboratory of Computational Science at the Sun Yat-sen University.

A Subdivision matrices

The 1-ring subdivision matrix $\mathbf{S}$

$$\mathbf{S}=\begin{pmatrix} \alpha & \frac{1-\alpha}{n} & \frac{1-\alpha}{n} & \cdots & \frac{1-\alpha}{n} \\ 1-\lambda_0 & \gamma_0 & \gamma_1 & \cdots & \gamma_{n-1} \\ 1-\lambda_0 & \gamma_{n-1} & \gamma_0 & \cdots & \gamma_{n-2} \\ \vdots & \vdots & \vdots & \ddots & \vdots \\ 1-\lambda_0 & \gamma_1 & \gamma_2 & \cdots & \gamma_0 \end{pmatrix}.$$

The remaining four blocks of $\bar{\mathbf{A}}$ are

$$\mathbf{S}_{11}=\frac{1}{16}\begin{pmatrix} 2 & 6 & 0 & 0 & \cdots & 0 & 0 & 6 \\ 1 & 10 & 1 & 0 & \cdots & 0 & 0 & 1 \\ 2 & 6 & 6 & 0 & \cdots & 0 & 0 & 0 \\ 1 & 1 & 0 & 0 & \cdots & 0 & 1 & 10 \\ 2 & 0 & 0 & 0 & \cdots & 0 & 6 & 6 \end{pmatrix} \quad \text{and} \quad \mathbf{S}_{12}=\frac{1}{16}\begin{pmatrix} 2 & 0 & 0 & 0 & 0 \\ 1 & 1 & 1 & 0 & 0 \\ 0 & 0 & 2 & 0 & 0 \\ 1 & 0 & 0 & 1 & 1 \\ 0 & 0 & 0 & 0 & 2 \end{pmatrix},$$

$$\mathbf{S}_{21}=\frac{1}{8}\begin{pmatrix}0&3&0&0&\cdots&0&0&1\\0&3&0&0&\cdots&0&0&0\\0&3&1&0&\cdots&0&0&0\\0&1&0&0&\cdots&0&0&3\\0&0&0&0&\cdots&0&0&3\\0&0&0&0&\cdots&0&1&3\end{pmatrix} \quad \text{and} \quad \mathbf{S}_{22}=\frac{1}{8}\begin{pmatrix}3&1&0&0&0\\1&3&1&0&0\\0&1&3&0&0\\3&0&0&1&0\\1&0&0&3&1\\0&0&0&1&3\end{pmatrix}.$$

References

[1] M. Abkarian, M. Faivre, and A. Viallat. Swinging of red blood cells under shear flow. Phys. Rev. Lett., 98:188302, 2007.

[2] D. Barthès-Biesel and J.M. Rallison. The time-dependent deformation of a capsule freely suspended in a linear shear flow. J. Fluid Mech., 113:251–267, 1981.

[3] G.K. Batchelor and J.T. Green. The hydrodynamic interation of two small freely-moving spheres in a linear flow field. J. Fluid Mech., 56:375–400, 1972.

[4] G. Breyiannis and C. Pozrikidis. Simple shear flow of suspensions of elastic capsules. Theor. and Comp. Fluid Dyn., 13:327–347, 2001.

[5] R. Charles and C. Pozrikidis. Significance of the dispersed-phase viscosity on the simple shear flow of suspensions of two-dimensional liquid drops. J. Fluid Mech., 365:205–234, 1998.

[6] J.M. Charrier, S. Shrivastava, and R. Wu. Free and constrained inflation of elastic membranes in relation to thermoforming nonaxisymmetric problems. J. Strain Anal., 24:55–74, 1989.

[7] F. Cirak and M. Ortiz. Fully C^1-conforming subdivision elements for finite deformation thin-shell analysis. Int. J. Numer. Meth. Engng., 51:813–833, 2001.

[8] F. Cirak, M. Ortiz, and P. Schroder. Subdivision surfaces: a new paradigm for thin-shell finite-element analysis. Int. J. Numer. Meth. Engng., 47:2039–2072, 2000.

[9] C.L. Darabaner and S.G. Mason. Particle motions in sheared suspensions xxii: Interaction of rigid spheres (experimental). Rheol. Acta, 6:273–284, 1967.

[10] S.K. Doddi and P. Bagchi. Effect of inertia on the hydrodynamic interaction between two liquid capsules in simple shear flow. Int. J. Multiphase Flow, 34:375–392, 2008.

[11] S.K. Doddi and P. Bagchi. Three-dimensional computational modeling of multiple deformable cells flowing in microvessels. Phys. Rev. E, 79:046318, 2009.

[12] C.D. Eggleton and A.S. Popel. Large deformation of red blood cell ghosts in a simple shear flow. Phys. Fluids, 10:1834–1845, 1998.

[13] T. M. Fischer. Shape memory of human red blood cells. Biophys. J., 86:3304–3313, 2004.

[14] W. Helfrich. Elastic properties of lipid bilayers: theory and possible experiments. Z. Naturforsch, 28:693–703, 1973.

[15] J. M. Higgins, D. T. Eddington, S. N. Bhatia, and L. Mahadevan. Statistical dynamics of flowing red blood cells by morphological image processing. PloS Computational Biology, 5:e1000288, 2009.

[16] W.X. Huang, C.B. Chang, and H.J. Sung. Three-dimensional simulation of elastic capsules in shear flow by the penalty immersed boundary method. J. Comput. Phys., 231:3340–3364, 2012.

[17] D.J. Jeffrey and Y. Onishi. Calculation of the resistance and mobility functions for two unequal rigid spheres in low-Reynolds-number flow. J. Fluid Mech., 139:261–290, 1984.

[18] E. Lac and D. Barthès-Biesel. Pairwise interaction of capsules in simple shear flow: Three-dimensional effects. Phys. Fluid, 20:040801, 2008.
[19] E. Lac, A. Morel, and D. Barthès-Biesel. Hydrodynamic interaction between two identical capsules in simple shear flow. J. Fluid Mech., 573:149–169, 2007.
[20] D.V. Le. Effect of bending stiffness on the deformation of liquid capsules enclosed by thin shells in shear flow. Phys. Rev. E, 82:016318, 2010.
[21] D.V. Le. Subdivision elements for large deformation of liquid capsules enclosed by thin shells. Comput. Methods Appl. Mech. Engrg., 199:2622–2632, 2010.
[22] D.V. Le and Z. Tan. Large deformation of liquid capsules enclosed by thin shells immersed in the fluid. J. Comput. Phys., 229:4097–4116, 2010.
[23] X. Li and K. Sarkar. Front tracking simulation of deformation and buckling instability of a liquid capsule enclosed by an elastic membrane. J. Comput. Phys., 227:4998–5018, 2008.
[24] M. Loewenberg and E. J. Hinch. Collision of two deformable drops in shear flow. J. Fluid Mech., 338:299–315, 1997.
[25] Charles Loop. Triangle mesh subdivision with bounded curvature and the convex hull property. Technical Report MSR-TR-2001-24, Microsoft Corporation, February 2001.
[26] C.T. Loop. Smooth subdivision surfaces based on triangles. Master's thesis, Department of Mathematics, University of Utah, 1987.
[27] J.E. Marsden and T.J.R Hughes. Mathematical Foundations of Elasticity. Prentice-Hall: Englewood Cliffs, NJ, 1983.
[28] C.S. Peskin. The immersed boundary method. Acta Numerica, 11(2):479–517, 2002.
[29] C. Pozrikidis. Effect of membrane bending stiffness on the deformation of capsules in simple shear flow. J. Fluid Mech., 440:269–291, 2001.
[30] C. Pozrikidis. Interception of two spheroidal particles in shear flow. J. Non-Newt. Fluid Mech., 136:50–63, 2006.
[31] C. Pozrikidis. Interception of two spherical particles with arbitrary radii in simple shear flow. Acta Mech., 194:213–231, 2007.
[32] S. Ramanujan and C. Pozrikidis. Deformation of liquid capsules enclosed by elastic membrane in simple shear flow: large deformations and the effect of fluid viscosities. J. Fluid Mech., 361:117–143, 1998.
[33] S. Shrivastava and J. Tang. Large deformation finite element analysis of non-linear viscoelastic membranes with reference to thermoforming. J. Strain Anal., 28:31–51, 1993.
[34] J.C. Simo and D.D. Fox. On a stress resultant geometrically exact shell model. Part IV: variable thickness shells with through-the-thickness stretching. Comput. Methods Appl. Mech. Engrg., 81:91–126, 1990.
[35] R. Skalak, A. Tozeren, R.P. Zarda, and S. Chien. Strain energy function of red blood cell membranes. Biophys. J., 13:245–264, 1973.
[36] J.M. Skotheim and T.W. Secomb. Red blood cells and other nonspherical capsules in shear flow: Oscillatory dynamics and the tank-treading-to-tumbling transition. Phys. Rev. Lett., 98:078301, 2007.
[37] J. Stam. Fast evaluation of Loop triangular subdivision surfaces at arbitrary parameter values. In Computer Graphics (SIGGRAPH '98 Proceedings, CD-ROM supplement), 1998.
[38] Y. Sui, Y.T. Chew, P. Roy, and H.T. Low. A hybrid method to study flow-induced deformation of three-dimensional capsules. J. Comput. Phys., 227:6351–6371, 2008.